



RESEARCH ARTICLE

Performance Evaluation of SimPET-X, a PET Insert for Simultaneous Mouse Total-Body PET/MR Imaging

Kyeong Yun Kim,^{1,2} Jeong-Whan Son,² Kyuwan Kim,^{2,3} Yina Chung,² Ji Yong Park,^{1,4} Yun-Sang Lee,^{3,5} Guen Bae Ko,^{2,3} Jae Sung Lee^{1,2,3,5} 

¹Department of Biomedical Sciences, Seoul National University College of Medicine, Seoul, Korea

²Brightonix Imaging Inc., #1705, Seongsu-yeok SK V1 Tower, 25, Yeonmujang 5ga-gil, Seongdong-gu, Seoul, 04782, Korea

³Institute of Radiation Medicine, Medical Research Center, Seoul National University College of Medicine, Seoul, Korea

⁴Dental Research Institute, Seoul National University, Seoul, Korea

⁵Department of Nuclear Medicine, Seoul National University College of Medicine, 103 Daehak-ro, Jongno-gu, Seoul, 03080, Korea

Abstract

Purpose: In this study, a small animal PET insert (SimPET-X, Brightonix Imaging Inc.) for simultaneous PET/MR imaging studies is presented. This insert covers an 11-cm-long axial field-of-view (FOV) and enables imaging of mouse total-bodies and rat heads.

Procedures: SimPET-X comprises 16 detector modules to yield a ring diameter of 63 mm and an axial FOV of 110 mm. The detector module supports four detector blocks, each comprising two 4 × 4 SiPM arrays coupled with a 20 × 9 array of LSO crystals (1.2 × 1.2 × 10 mm³). The physical characteristics of SimPET-X were measured in accordance with the NEMA NU4-2008 standard protocol. In addition, we assessed the compatibility of SimPET-X with a small animal-dedicated MRI (M7, Aspect Imaging) and conducted phantom and animal studies.

Results: The radial spatial resolutions at the center based on 3D OSEM without and with the warm background were 0.73 mm and 0.99 mm, respectively. The absolute peak sensitivity of the system was 10.44% with an energy window of 100–900 keV and 8.27% with an energy window of 250–750 keV. The peak NECR and scatter fraction for the mouse phantom were 348 kcps at 26.2 MBq and 22.1% with an energy window of 250–750 keV, respectively. The standard deviation of pixel value in the uniform region of a NEMA IQ phantom was 4.57%. The spillover ratios for air- and water-filled chambers were 9.0% and 11.0%, respectively. In the hot-rod phantom image reconstructed using 3D OSEM-PSF, all small rods were resolved owing to the high spatial resolution of the SimPET-X system. There was no notable interference between SimPET-X and M7 MRI. SimPET-X provided high-quality mouse images with superior spatial resolution, sensitivity, and counting rate performance.

Conclusion: SimPET-X yielded a remarkably improved sensitivity and NECR compared with SimPETTM.

Key words: PET/MRI, Animal PET, Molecular imaging, Instrumentation

Introduction

Positron emission tomography (PET) and magnetic resonance imaging (MRI) provide unique opportunities to obtain

Correspondence to: Guen Ko; e-mail: guenko@gmail.com, Jae Lee; e-mail: jaes@snu.ac.kr

functional and structural information non-invasively from living bodies [1–4]. PET allows for highly sensitive assessment of functional and molecular processes in biological systems, while MRI offers superior soft-tissue contrast compared with X-ray computed tomography (CT) [5–8]. PET/MR imagers based on advanced semiconductor photosensors that collect the scintillation lights in PET detectors allow for simultaneous PET/MRI scanning with an insignificant performance compromise for each imaging modality [9–16]. In preclinical small animal studies, simultaneous scans have several advantages over sequential scans, including reduced scan time and anesthesia use, better spatial correlation between multimodality images, and concurrent assessment of different biological parameters [7, 11].

SimPET™ (Brightonix Imaging Inc., Seoul, South Korea) is a silicon photomultiplier (SiPM)-based PET insert for simultaneous PET/MR imaging with a compact design and low power consumption [17]. The SimPET™ scanner has inner and outer diameters of 6.0 and 9.9 cm, respectively, allowing for a combination with animal-dedicated MR systems with a bore size larger than 10 cm. The small scintillation crystal element size ($1.2 \times 1.2 \times 10 \text{ mm}^3$) and detector ring diameter (6.3 cm) of SimPET™ yield reconstructed images with high spatial resolutions (0.7 mm and 1.45 mm at the center based on three-dimensional ordered-subset expectation maximization (OSEM) without and with a warm background). The long axial field-of-view (FOV) of SimPET™ (5.5 cm) and its high geometric efficiency in detecting annihilation photon pairs allow for a high peak sensitivity (4.21%) and noise-equivalent count rate (151 kcps at 38.4 MBq) with an energy window of 250–750 keV. However, the 5.5-cm axial FOV is not sufficiently long for simultaneous PET/MRI scanning of a mouse total body in a single-bed position.

Imaging the entire body in a single-bed position without moving an object allows for the assessment of the fast whole-body biodistribution changes of radiotracers [18, 19]. In addition, the high geometric efficiency of the total-body, long-axial-FOV PET scanners lead to improved system sensitivity and image quality, allowing for reduced radiotracer use and/or scan time. In a previous study, a preclinical PET system that extends the axial FOV by reusing the detectors of a clinical PET scanner permitted very-low-activity scans of nonhuman primates using ^{89}Zr , a radioisotope with low positron abundance [20]. Early human studies with total-body PET scanners have also demonstrated their potential benefits for both clinical and research applications [18].

SimPET-X (Brightonix Imaging) is a newly developed small animal PET insert for simultaneous PET/MR scanners, covering an 11-cm-long axial FOV and enabling imaging of mouse total-bodies and rat heads. Relative to the previous SimPET™ scanner, the axial FOV was doubled in SimPET-X (Table 1). In addition, the size of the scintillation crystal array increased from 9×9 to 20×9 , which further enhanced

the sensitivity of annihilation photon detection. To effectively process the large amounts of data resulting from the remarkably improved sensitivity, the shape of the analog signal output from the SiPM array was optimized. Moreover, reconstruction algorithms were accelerated using a graphical processing unit (GPU). In this study, we measured the physical performance of SimPET-X in accordance with the National Electrical Manufacturers Association (NEMA) NU4-2008 protocol and assessed its compatibility with the M7 MRI scanner manufactured by Aspect Imaging (Shoham, Israel). We also conducted phantom and animal studies to demonstrate the feasibility of the new PET insert and the benefits of the improved sensitivity.

Materials and Methods

System Description

The specifications of SimPET-X and SimPET™ are compared in Table 1. The SimPET-X insert comprises 16 detector modules to yield a ring diameter of 63 mm and an axial FOV of 110 mm. The detector module supports four detector blocks, each of which comprises two 4×4 SiPM arrays (S14161-3050HS-04; Hamamatsu Photonics K.K., Japan) coupled with a 20×9 array of lutetium oxyorthosilicate (LSO) crystals ($1.2 \times 1.2 \times 10 \text{ mm}^3$) (Fig. 1). The ambient temperature of the detector was continuously monitored, and a regulated bias voltage was applied to the SiPM arrays to compensate for the temperature-dependent variation in the SiPM gain [21]. Anode signals from two 4×4 SiPM arrays were multiplexed to four position signals through a resistive charge division network [21–23]. Accordingly, the ratio of analog multiplexing enabled by the resistive charge division network of SimPET-X is 32:4, which is twice that of SimPET™ (16:4). However, the pulse width degradation caused by the increased multiplexing ratio (increased pulse width leading to count rate performance degradation) was mitigated by applying pole-zero cancellation filtering to the multiplexed position signals [Fig. 2(a)] [24]. The higher multiplexing ratio of SimPET-X with a shortened pulse width enables the use of the same subsequent signal processing and readout electronics as in SimPET™.

Data Acquisition and Processing

The number of readout channels from the detector blocks was further reduced using a bipolar multiplexing technique [25]. The multiplexed signals were digitized using analog-to-digital converters with a 125-MHz sampling rate. A data acquisition system based on a field-programmable gate array was used to process the digitized signals to extract energy, timing, and position information [26]. Prompt and delay coincidences filtered by the energy and time windows were then transferred to a computer through 1-Gbps Ethernet.

Table 1. Specification comparison between SimPETTM and SimPET-X

		SimPET TM [17]	SimPET-X
Detector	Scintillator material	LSO	
	Crystal size (mm ³)	1.2×1.2×10	
	Crystal pitch (mm)	1.28	
	Crystal array	9×9	20×9
	SiPM* array	4×4	8×4
System	No. of crystal rings	36	80
	No. of crystals/ring	144	
	Detector face to face (mm)	63	
	Transaxial FOV† (mm)	50	
	Axial FOV† (mm)	55	110
	Overall dimensions Φ (cm) × L (cm)	9.9 × 61.5	

*SiPM silicon photomultiplier

†FOV field-of-view

System control and data acquisition were managed using the SOPHIA3 software. SOPHIA3 was used to visualize the accumulated counts from the animals in projection and reconstructed image spaces updated at predefined intervals during the PET scan. In addition, SOPHIA3 supported listmode data acquisition, which enables flexible post-acquisition time-binning of the acquired PET data.

Phantom and animal data were reconstructed using a three-dimensional ordered-subset expectation maximization (3D OSEM, 12 subsets, 3 iterations) algorithm with or without incorporating point spread function (PSF) models. The voxel size of the reconstructed images was $0.32 \times 0.32 \times 0.64$ mm³. The reconstruction was performed using a GPU to mitigate the computational burden caused by the increased axial FOV and the incorporated PSF modeling.

PET and MRI images were automatically registered using geometric transformation parameters obtained using a calibration phantom. MRI-segmentation-based attenuation correction was also performed. To generate the PET attenuation map, gradient echo (GRE) MR images of animals acquired with PET were automatically segmented into three classes (air, lung, and soft tissue), and known

attenuation coefficient for each class was assigned. Then, CT-based attenuation maps of RF coil and animal cradle were added to the attenuation map of animal.

Performance Evaluation

The system performance including spatial resolution, sensitivity, count-rate performance, and image quality, was evaluated in accordance with the NEMA NU4-2008 standard protocol outside MR magnet.

Spatial Resolution

A ²²Na point source (0.49 MBq) embedded in a 10-mm acrylic cube was used to acquire data for spatial resolution measurement. The point source was scanned while it was located at 0, 5, 10, and 15 mm from the center of the transaxial FOV at the center of the axial FOV. The measurements were repeated at the same radial positions at a distance one-fourth of the axial FOV. In each position,

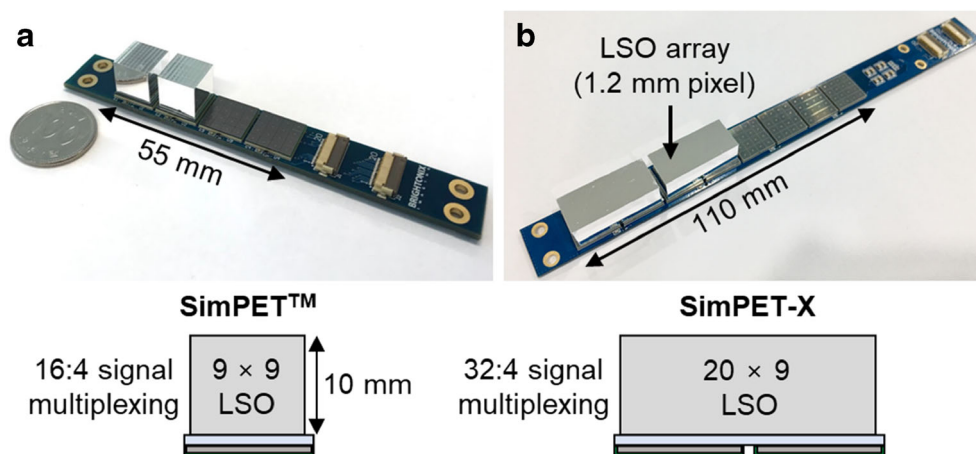


Fig. 1. Comparison of detector modules of SimPETTM (left) and SimPET-X (right). The SimPET-X has an axial field-of-view two times longer than that of SimPETTM, because twice as many SiPM arrays and 2.2 times more scintillation crystal elements are used in SimPET-X. The increased number of SiPM signal channels results in the higher signal multiplexing ratio in SimPET-X.

PET data were acquired for 5 min with a 350–650 keV energy window and reconstructed using the 3D OSEM algorithm (3 iterations and 12 subsets). The full width at half maximum (FWHM) and full width at tenth maximum were calculated using the method specified in the NEMA standard. Additionally, the spatial resolution measurement was repeated after addition of a 10% warm background to the point-source data. The filtered backprojection reconstruction specified in NEMA NU4 was not applied, because the reconstruction method causes an ambiguous spatial resolution depending on the size of the projection window and the anisotropic spatial resolution, due to serious star-like artifacts appearing in reconstructed images [27].

Sensitivity

The axial sensitivity profile was obtained using the same ^{22}Na point source as that used for the spatial resolution measurement. The point source was placed at the center of the transaxial FOV and axially moved in steps of 0.64 mm. Data at each position were collected for 1 min using four different energy windows (100–900 keV, 250–750 keV, 350–650 keV, and 400–600 keV). Absolute sensitivities were calculated as described in the NEMA standard.

Count-Rate Performance

The count-rate performance was measured using the NEMA NU-4 2008 mouse-like phantom (length of 70 mm and diameter of 25 mm) in the 250–750-keV energy window. The phantom was placed at the center of PET FOV. A 60-mm-long line source with an outer diameter that fits into the 3.2-mm hole of the phantom was filled with 140 MBq ^{18}F solution. Listmode data were acquired for 10 min at 10-min intervals over 24 h and processed as described in the NEMA protocol to estimate the prompt, random, scatter, and true event rates and the noise-equivalent count rate (NECR). The scatter fraction was determined using the data acquired during the last 10 min, with random event rates below 1.0% of the true event rate.

Image Quality

An image quality (IQ) phantom described in the NEMA NU4-2008 was filled with 3.7 MBq of ^{18}F solution and scanned for 20 min with a 400–600-keV energy window at the center of the FOV. Image uniformity, resolution recovery coefficients, and the accuracy of corrections were analyzed according to the standard. In addition, a hot-rod resolution phantom containing six wedges of activity-filled rods with diameters of 0.75, 1.0, 1.35, 1.7, 2.0, and 2.4 mm was scanned to estimate the spatial resolution. The hot-rod resolution phantom was reconstructed using 3D OSEM-PSF (16 iterations and 12 subsets).

MR Compatibility

To assess the potential mutual interference between PET and MRI, SimPET-X was combined with Aspect Imaging's M7 MR scanner using a 1-T magnet. The influence of the PET insert on MRI measurement was explored by scanning a uniform cylinder phantom filled with a solution of CuSO_4 and NaCl mixed in water using various MRI pulse sequences that are routinely employed in animal studies: 3D GRE, T1-weighted spin echo (T1W SE), and T2-weighted fast spin echo (T2W FSE); the power of SimPET-X was turned on or off during the scanning. The integral uniformity and signal-to-noise ratio (SNR) of the MR images were calculated in accordance with our previous study [11, 17].

The influence of MRI on PET was also assessed by measuring the blank PET count rate under the 3D GRE, T1W SE, and T2W FSE MRI pulse sequences. All sequence parameters were identical to those in routine mouse studies, except for the number of excitations, to enable a scan time longer than 5 min. The prompt and delayed coincidence rates triggered by the intrinsic activity of ^{176}Lu of the LSO crystal and determined by applying default energy and time windows were measured with or without MR sequences to explore whether the MR pulse sequences caused false triggering of PET coincidence detection.

Animal Imaging Studies

Mouse imaging studies were performed to explore the advantage of the total-body imaging capability and high sensitivity of SimPET-X integrated with M7 MRI. All animal studies were approved by the Institutional Animal Care and Use Committee at the Seoul National University Hospital. During the image studies, mice were laid on a heated animal-handling system in a prone position while being anesthetized with isoflurane (1.5–3% in air).

The whole body of a 16.2-g BALB/c mouse was scanned 30 min after intravenous injection of 10.0-MBq ^{18}F -NaF for 10 min. Another mouse (weight = 16.5 g) was scanned following the same protocol, except for the injection dose being 0.15 MBq, to determine the potential for very-low-activity scanning of mice using SimPET-X. In addition, a total-body dynamic PET scan was performed on a BALB/c mouse (weight = 16.1 g). The dynamic scan was started simultaneously with the intravenous injection of 12.2 MBq ^{18}F -FDG. During the scan, the listmode data were acquired in a single-bed position for 40 min. The listmode data were then divided into 98 temporal frames with variable frame durations (2 sec \times 30, 4 sec \times 30, 15 sec \times 8, 30 sec \times 10, and 60 sec \times 30). The PET images were acquired inside the MR magnet without an RF coil.

A mouse brain imaging study was also conducted to demonstrate the feasibility of simultaneous PET/MRI studies using SimPET-X and M7 scanners. We intravenously

injected ^{18}F -FDG of 12.6 MBq via the tail vein into a 17.1-g BALB/c mouse and performed a 40-min PET/MRI scan after a 45-min tracer uptake period. T2W FSE (TR/TE = 3250/68.7 ms, echo train length [ETL] = 12) MR images were simultaneously acquired with ^{18}F -FDG for 40 min. Spatial registration parameters between the PET and MR images that were previously derived through a calibration phantom study were applied to the images.

Results

Detector Performance

Figure 2 depicts the intrinsic performance of a typical SimPET-X detector block. The pulse width of the multiplexed position signals was approximately 260 ns before application of the pole-zero cancellation filter [Fig. 2(a)]. The pulse width was longer than that of a typical SimPETTM detector block (~190 ns). By applying the pole-zero cancellation filters to the multiplexed signals, the pulse width was remarkably reduced (~85 ns), which ensured

improved count-rate performance. Pulse width was defined as the time from the 10% threshold of the rising edge of the pulse to the 10% threshold of the next falling edge. The pulse widths were averaged over 1,000 pulses.

All 1.2-mm crystals in the detector block were well resolved in the flood map [Fig. 2(b)]. For all 11,520 crystals, the average photo-peak position and energy resolution at 511 keV were $15,234 \pm 1,048$ (a.u.) and $10.1 \pm 0.8\%$ (mean \pm stand deviation), respectively. The peak positions of the energy spectrum and the energy resolution measured at each crystal element were uniform, except for the crystals on the boundary of the SiPM arrays [Fig. 2(c)]. The worst crystal-level energy resolution at the boundary was less than 15%.

System Performance

The radial spatial resolutions at the axial center measured using the 3D OSEM algorithm without the warm background were 0.73 mm and 2.14 mm FWHM at the transaxial center and 15-mm off-center position, respectively [Fig.

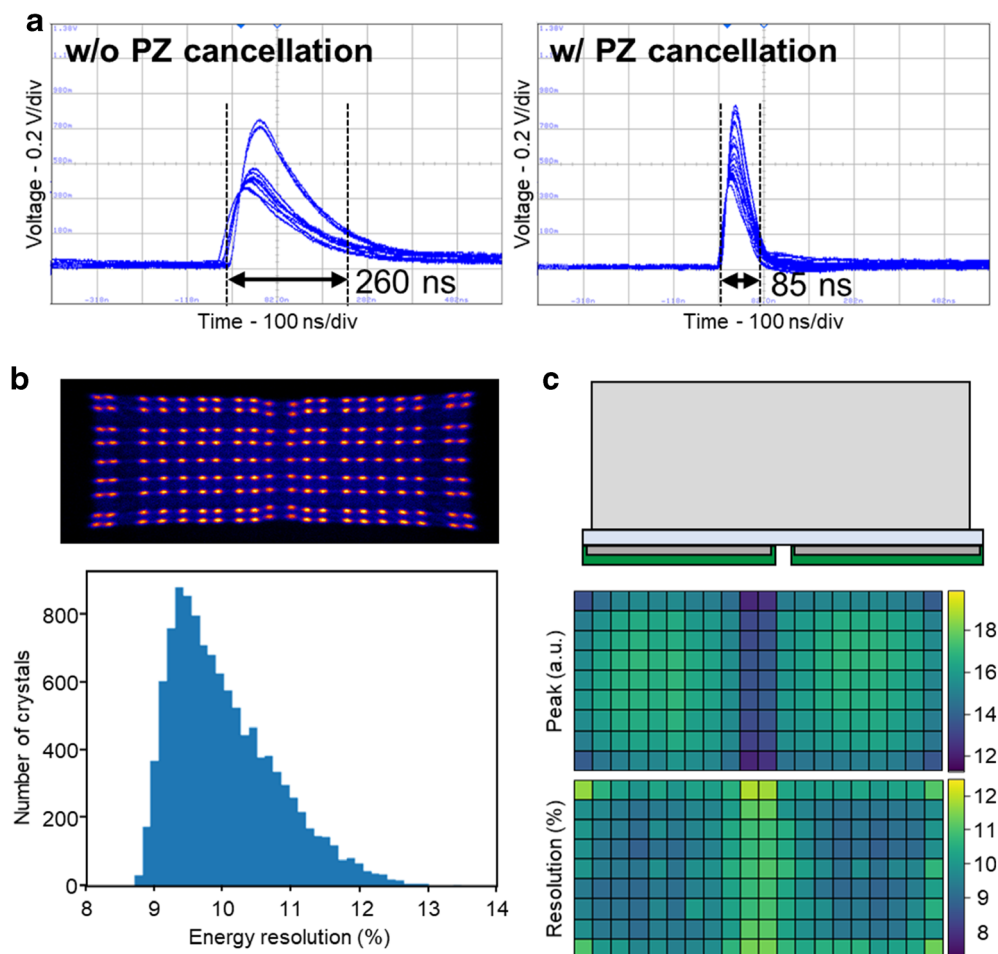


Fig. 2. Performance of a typical detector block. (A) Multiplexed position signals from a detector block (before and after applying pole-zero cancellation filtering). (B) Flood map and histogram of crystal-level energy resolution. (C) Peak position in the energy spectrum and energy resolution of each crystal element.

3(a)]. The radial resolution remained under 1.2 mm within 15 mm from the center when OSEM-PSF was applied. Adding a 10% warm background to the point-source data resulted in degradation of the spatial resolution [Fig. 3(b)]. Detailed results from the spatial resolution measurement are summarized in Supplemental Tables 1–4.

The absolute peak sensitivity of the system was 10.44% with an energy window of 100–900 keV and 8.27% with an energy window of 250–750 keV [Fig. 4(a)]. The average sensitivity over the axial FOV of ± 25 mm from the center was 7.12% for 250–750 keV, which represents a 143% improvement compared with the 2.93% sensitivity of SimPETTM. The peak NECR and scatter fraction for the mouse phantom were 348 kcps at 26.2 MBq and 22.1% with an energy window of 250–750 keV [Fig. 4(b)]. The peak NECR was improved by approximately 130% compared with the SimPETTM system.

Figure 5 shows the reconstructed images of the phantoms. The standard deviation of the pixel values in the uniform region of the NEMA IQ phantom shown in Fig. 5(a) was 4.57%, and the recovery coefficients of five different hot-rods were 0.13, 0.56, 0.81, 0.91, and 0.90 for 1-, 2-, 3-, 4-, and 5-mm rod diameters, respectively. The spillover ratios for air- and water-filled chambers were 9.0% and 11.0%, respectively. In the hot-rod phantom image reconstructed using 3D OSEM-PSF, all small rods were resolved owing to the high spatial resolution of the SimPET-X system [Fig. 5(b)].

The system performance of SimPETTM and SimPET-X is compared in Table 2. The point-source spatial resolution, uniformity, and recovery coefficients in the NEMA IQ phantom measured using SimPET-X were virtually equivalent to those measured using SimPETTM. SimPET-X yielded a remarkably improved sensitivity and NECR compared with SimPETTM. In addition, SimPET-X exhibited smaller spillover ratios in air and water relative to SimPETTM.

MR Compatibility

There were no significant differences in the MR image intensity level, SNR, and uniformity with and without the SimPET-X insert, as shown in Fig. 6 and Table 3. In addition, whether the PET was turned on or off did not affect

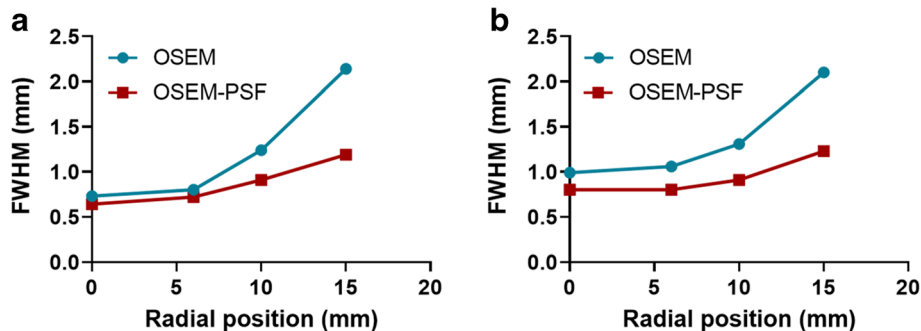


Fig. 3. Radial spatial resolution of SimPET-X scanner obtained using 3D OSEM and OSEM-PSF. (A) Without a warm background. (B) With a warm background.

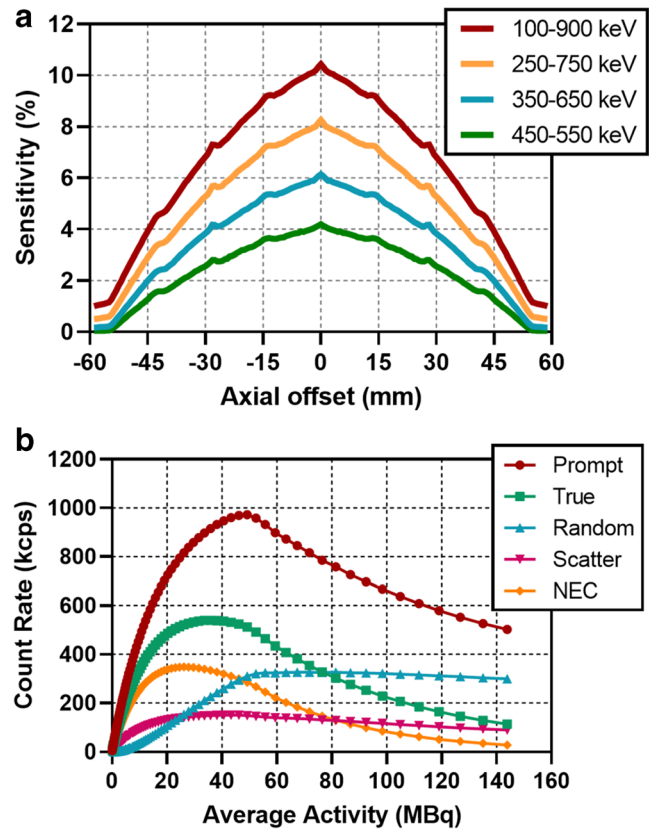


Fig. 4. Sensitivity and count-rate performance. (A) Axial sensitivity profiles at the center of transaxial field-of-view measured with different energy windows. (B) Different event types as a function of the total activity within the NEMA mouse-like phantom (energy window = 250–750 keV).

the MR images. Moreover, there was no remarkable change ($<1\%$) in the blank PET count rate when various MRI pulse sequences were applied.

Imaging Studies

Figure 7(a) shows the maximum-intensity projection images of ^{18}F -NaF, highlighting the benefit of the high sensitivity of

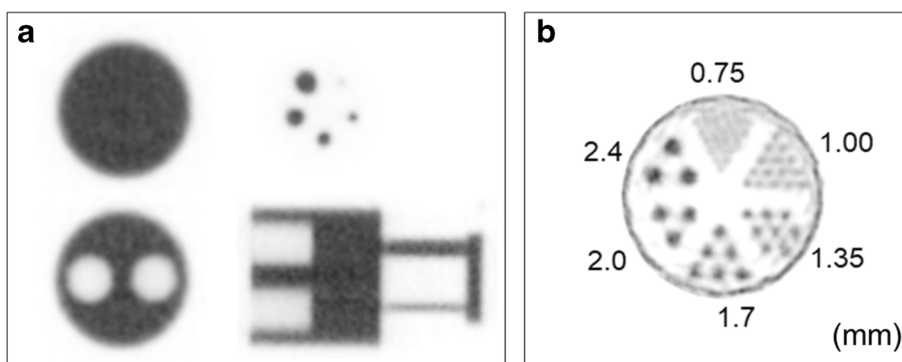


Fig. 5. Phantom images. (A) NEMA IQ phantom image. (B) Hot-rod phantom.

SimPET-X. The detailed bone structures of a mouse are clearly demonstrated both in the typical-dose and very-low-dose conditions (10.0 MBq and 0.15 MBq, respectively). Figure 7(b) shows five selected frames from a 40-min dynamic PET scan performed following the tail vein injection of 12.2-MBq ^{18}F -FDG, demonstrating the total-body dynamic imaging capability of SimPET-X without movement of the animal bed. No visible artifacts were observed in the simultaneous PET/MRI scan of the mouse brain [Fig. 7(c)]. The PET images depict a high cortical uptake of ^{18}F -FDG in the brain, and the 1-T MR image provides a high soft-tissue contrast, which is useful for examining activity distribution in the mouse brain.

Discussion

In this study, SimPET-X, an MR-compatible PET system with an 11-cm-long axis FOV, was described and evaluated. The SimPET-X systems were characterized in accordance with the NEMA NU4-2008 standard and compared with the previous SimPETTM system. Furthermore, we integrated the SimPET-X system into an M7 MR scanner to assess its MR

compatibility for simultaneous PET and MRI scans of small animals.

The new detector module used in SimPET-X was designed to mount $2\times$ more SiPM and $2.2\times$ more scintillation crystal elements than the detector module for SimPETTM; thus, SimPET-X yields an approximately $2.4\times$ higher sensitivity than SimPETTM does. To maintain compatibility with existing signal-processing and readout electronics, the multiplexing ratio of the detector blocks was increased to 32:4. Increasing the multiplexing ratio can lead to a longer output pulse width, which can degrade the count-rate performance of PET systems. In this study, we applied the pole-zero cancellation technique to the multiplexed signal, which resulted in a shorter pulse width than that of the previous system, as well improved count-rate performance (peak NECR with 250–750 keV energy window: 151 kcps in SimPETTM and 348 kcps in SimPET-X).

In SimPET-X, we implemented the PSF reconstruction technique to achieve a sub-millimeter spatial resolution in the full FOV. However, incorporating the PSF kernel into the system response matrix increased the computational burden. A $2\times$ increase in axial FOV also requires $8\times$ more

Table 2. Performance comparison between SimPETTM and SimPET-X

		SimPET TM [17]	SimPET-X
Radial resolution at center	OSEM* (mm)	0.70	0.73
	OSEM-PSF (mm)	N.A.	0.64
Sensitivity	100–900 keV (%)	N.A.	10.44
	250–750 keV (%)	4.21	8.27
	350–650 keV (%)	3.10	6.14
	400–600 keV (%)	2.70	5.32
	Peak NECR† (kcps)	151	348
Count-rate performance (250–750 keV)	Activity at peak NECR (MBq)	38.4	26.2
	Scatter fraction (%)	22.0	22.1
	Uniformity (%)	4.42	4.57
Image quality	RC‡ at 1-, 2-, 3-, 4-, and 5- rod diameter	0.17, 0.52, 0.75, 0.85, 0.90	0.13, 0.56, 0.91, 0.91, 0.90
	SOR§ air (%)	12.7	9.0
	SOR§ water (%)	14.6	11.0

*OSEM ordered-subset expectation maximization

†NECR noise-equivalent count rate

‡RC recovery coefficient

§SOR spillover ratio

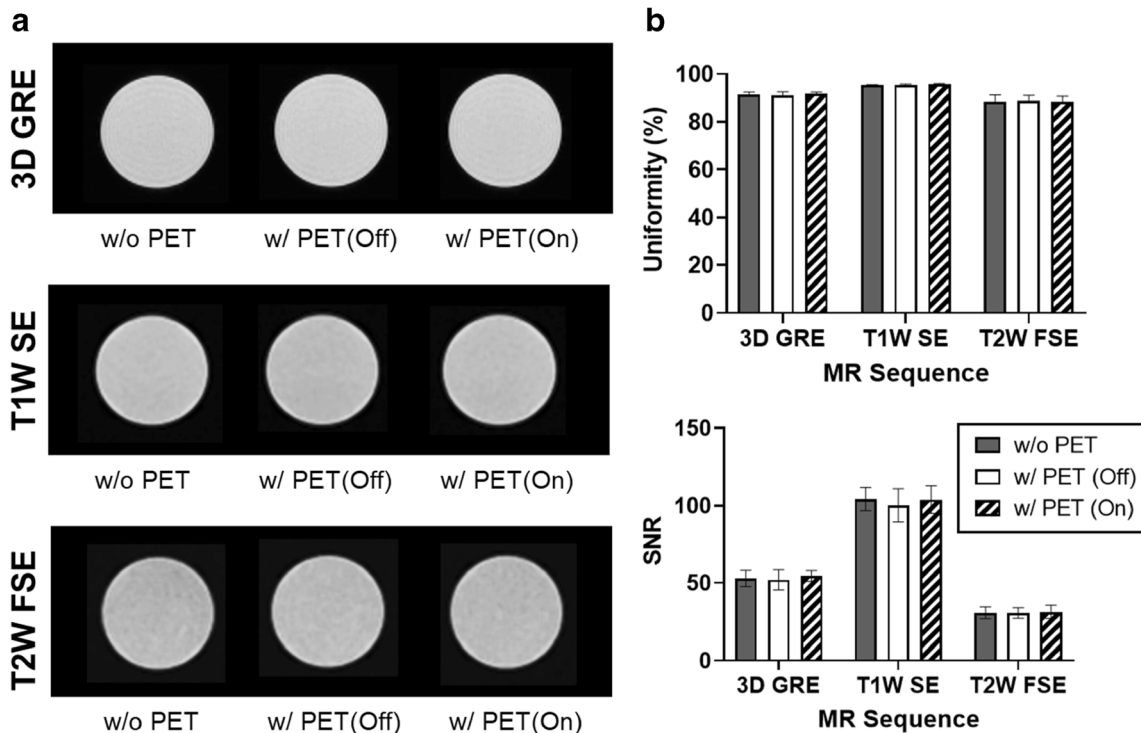


Fig. 6. MRI compatibility of SimPET-X. (A) MR images acquired using various MRI pulse sequences under different PET conditions. (B) Uniformity and SNR of the MR images.

computation during reconstruction. Parallelization using a GPU accelerates forward and backward projection in image reconstruction, increasing the reconstruction speed by 10 times compared with using a multi-threaded CPU. We intend to improve the reconstruction process further by optimizing the cache, memory, and job scheduling as well as by implementing advanced algorithms with fast-convergence properties.

The main advantages of the high sensitivity and spatial resolution of SimPET-X are the superior image quality of phantom and animal images. In image quality measurements in accordance with the NEMA NU4-2008 standard, SimPET-X yielded higher recovery coefficients and lower spillover ratios than SimPETTM did while maintaining a level of high spatial resolution (0.7/0.73 mm) and image uniformity (4.42/4.57) and providing significantly improved NECR (151/348 kcps). The higher recovery coefficient and lower spillover ratio, the better image contrast. In addition, SimPET-X provided a high-SNR image with only a single-bed scan, even when the injected activity was low or when the scan time frame was short. Total-body mouse imaging with no bed motion, which is possible in SimPET-X, would be useful for capturing the fast tracer dynamics during the early phase of tracer uptake and for estimating the arterial input function derived from images [28–30].

There was no notable interference between SimPET-X and M7 MRI during evaluation using a uniform phantom, and animal studies with ¹⁸F-FDG demonstrated the feasibility of simultaneous PET/MR imaging based on the SimPET-

X/M7 combination. M7 MR images with a high spatiotemporal correlation with SimPET-X images will allow for more accurate identification of regions of interest. The same PET insert with larger diameter (ID=7.6 cm) is also used together with Bruker 9.4T MRI (LB1026, World Molecular Imaging Congress 2020). The integrated PET/MRI systems will be useful for investigating the pathophysiology of a disease, efficacy of treatment strategies, and characteristics of new tracers.

The specification and performance of commercially available MR-compatible PET systems that allow the mouse total-body imaging are summarized in Table 4. They commonly use SiPM and LSO or LYSO scintillation crystals. The thickness of the crystal is commonly 10 mm.

Table 3. MRI compatibility of SimPET-X: Uniformity and SNR of the MR images

		w/o PET	w/ PET (Off)	w/ PET (On)
Uniformity	3D GRE*	91.5±1.00	91.0±1.50	91.8±0.66
	T1W SE†	95.3±0.33	95.3±0.51	95.6±0.43
	T2W FSE‡	88.4±2.90	88.7±2.40	88.6±2.15
SNR	3D GRE*	53.0±5.28	52.0±6.58	54.6±3.47
	T1W SE†	104±7.43	100±10.73	104±8.92
	T2W FSE‡	30.7±3.71	30.5±3.36	31.3±4.21

*3D GRE 3-dimensional gradient-echo

†T1W SE T1-weighted spin-echo

‡T2W FSE T2-weighted fast spin-echo

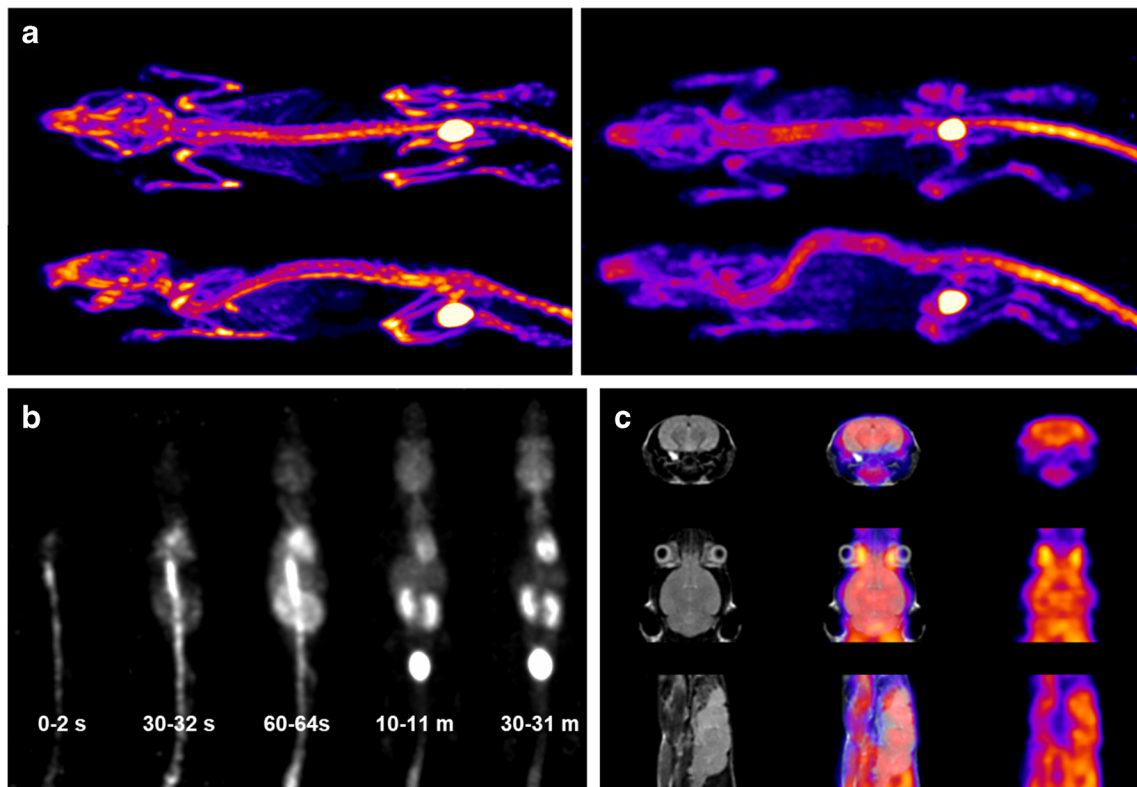


Fig. 7. Mouse imaging studies. **(A)** Maximum-intensity projection images acquired 30 min after the intravenous injection of ^{18}F -NaF with different activity levels (left: 10.0 MBq; right: 0.15 MBq). **(B)** Five selected frames from a 40-min dynamic PET scan performed following the injection of 12.2-MBq ^{18}F -FDG. **(C)** Simultaneous PET/MR imaging (^{18}F -FDG PET and T2W FSE MRI).

The Bruker Si 198 system uses monolithic crystals (50×50 mm), while the other systems use pixelated crystals. SimPET-X has a smaller crystal pitch than MR Solutions PET INSERT (1.28 mm vs. 1.68 mm). SimPET-X and Si 198 provide <0.7 mm spatial resolution at the center of FOV when iterative reconstruction algorithms (OSEM or MLEM) incorporating PSF are applied. All of them feature high sensitivity and peak NECR.

One of the limitations of this study is that the effect of MRI on the PET system was only addressed by the

count rate, and the performance evaluation of SimPET-X was done only outside the magnet. Therefore, more extensive MRI compatibility investigations are left for future research. The future research should investigate the impact of MR components and MRI pulse sequences on PET performance, including timing resolution, energy resolution, spatial resolution, sensitivity, and image quality. In addition, the performance evaluations could be repeated in the magnet with and without the MR coils in place.

Table 4. Comparison of Commercially available MR-compatible mouse total-body PET systems

		Brightonix SimPET-X	Bruker Si 198 (3 Rings)	MR Solutions PET INSERT
PET specification	Detector face to face (mm)	63	114	116
	Axial FOV* (mm)	110	150	102.5
Radial resolution at center	Iterative (mm)	0.73		
	Iterative-PSF (mm)	0.64	0.68	
	FBP (mm)			1.74
Sensitivity‡		8.27	11	7.9
Count-rate performance (mouse)‡	Peak NECR† (kcps)	348	486	426.9
	Activity at peak NECR (MBq)	26.2	22.6	34.3
Reference		This study	[31]	[32]

*FOV field-of-view

†NECR noise-equivalent count rate

‡Measured with the energy window of 250–750 keV

Conclusions

To provide an 11-cm-long axial FOV, the SimPET-X system was evaluated based on NEMA NU4-2008 standard measurements. Owing to a uniform spatial resolution and its superior sensitivity and counting rate performance, SimPET-X provided high-quality phantom and mouse images. The feasibility of simultaneous PET/MR imaging studies using a combination of SimPET-X with the M7 MRI scanner was also demonstrated.

Supplementary Information. The online version contains supplementary material available at <https://doi.org/10.1007/s11307-021-01595-z>.

Funding. This work was supported in part by grants from the Korean Ministry of SMEs and Startups (grant no. S2580037), the Korea Medical Device Development Fund (202011A06-1), and the National Research Foundation of Korea (NRF) funded by the Ministry of Education (NRF-2018R1D1A1B07045559).

Declarations

Ethics Approval

All animal experiments were approved by the Institutional Animal Care and Use Committee at the Seoul National University Hospital.

Conflict of Interest

KY Kim, J-W Son, K Kim, Y Chung, GB Ko, and JS Lee are employees of Brightonix Imaging Inc.

References

- Pomper MG, Lee JS (2005) Small animal imaging in drug development. *Curr Pharm Des* 11:3247–3272
- Yoo HJ, Lee JS, Lee JM (2015) Integrated whole body MR/PET: where are we? *Korean J Radiol* 16:32–49
- Balyasnikova S, Löfgren J, de Nijs R, Zamogilnaya Y, Højgaard L, Fischer BM (2012) PET/MR in oncology: an introduction with focus on MR and future perspectives for hybrid imaging. *Am J Nucl Med Mol Imaging* 2:458–474
- Kubiessa K, Purz S, Gawlitza M, Kühn A, Fuchs J, Steinhoff KG, Boehm A, Sabri O, Kluge R, Kahn T, Stumpp P (2014) Initial clinical results of simultaneous 18 F-FDG PET/MRI in comparison to 18 F-FDG PET/CT in patients with head and neck cancer. *Eur J Nucl Med Mol Imaging* 41:639–648
- Judenhofer MS, Wehr HF, Newport DF, Catana C, Siegel SB, Becker M, Thielscher A, Kneilling M, Lichy MP, Eichner M, Klingel K, Reischl G, Widmaier S, Röcken M, Nutt RE, Machulla HJ, Uludag K, Cherry SR, Claussen CD, Pichler BJ (2008) Simultaneous PET-MRI: a new approach for functional and morphological imaging. *Nat Med* 14:459–465
- Catana C, Procissi D, Wu Y, Judenhofer MS, Qi J, Pichler BJ, Jacobs RE, Cherry SR (2008) Simultaneous in vivo positron emission tomography and magnetic resonance imaging. *Proc Natl Acad Sci U S A* 105:3705–3710
- Pichler BJ, Kolb A, Nägele T, Schlemmer H-P (2010) PET/MRI: paving the way for the next generation of clinical multimodality imaging applications. *J Nucl Med* 51:333–336
- Karthik R, Radhakrishnan M, Rajalakshmi R, Raymann J (2020) Delineation of ischemic lesion from brain MRI using attention gated fully convolutional network. *Biomed Eng Lett* 11:3–13
- Yoon HS, Ko GB, Kwon SI, Lee CM, Ito M, Chan Song I, Lee DS, Hong SJ, Lee JS (2012) Initial results of simultaneous PET/MRI experiments with an MRI-compatible silicon photomultiplier PET scanner. *J Nucl Med* 53:608–614
- Yamamoto S, Watabe T, Watabe H et al (2011) Simultaneous imaging using Si-PM-based PET and MRI for development of an integrated PET/MRI system. *Phys Med Biol* 57:N1–N13
- Ko GB, Yoon HS, Kim KY, Lee MS, Yang BY, Jeong JM, Lee DS, Song IC, Kim SK, Kim D, Lee JS (2016) Simultaneous multiparametric PET/MRI with silicon photomultiplier PET and ultra-high-field MRI for small-animal imaging. *J Nucl Med* 57:1309–1315
- Levin CS, Maramraju SH, Khalighi MM, Deller TW, Delso G, Jansen F (2016) Design features and mutual compatibility studies of the time-of-flight PET capable GE SIGNA PET/MR system. *IEEE Trans Med Imaging* 35:1907–1914
- Hong SJ, Kang HG, Ko GB, Song IC, Rhee J-T, Lee JS (2012) SiPM-PET with a short optical fiber bundle for simultaneous PET-MR imaging. *Phys Med Biol* 57:3869–3883
- Schug D, Lerche C, Weessler B, Gebhardt P, Goldschmidt B, Wehner J, Dueppenbecker PM, Salomon A, Hallen P, Kiessling F, Schulz V (2016) Initial PET performance evaluation of a preclinical insert for PET/MRI with digital SiPM technology. *Phys Med Biol* 61:2851–2878
- Stortz G, Thiessen JD, Bishop D, Khan MS, Kozłowski P, Retière F, Schellenberg G, Shams E, Zhang X, Thompson CJ, Goertzen AL, Sossi V (2018) Performance of a PET insert for high-resolution small-animal PET/MRI at 7 tesla. *J Nucl Med* 59:536–542
- Hong SJ, Song IC, Ito M, Kwon SI, Lee GS, Sim KS, Park KS, Rhee JT, Lee JS (2008) An investigation into the use of Geiger-mode solid-state photomultipliers for simultaneous PET and MRI acquisition. *IEEE Trans Nucl Sci* 55:882–888
- Son J-W, Kim KY, Park JY, Kim K, Lee YS, Ko GB, Lee JS (2020) SimPET: a preclinical PET insert for simultaneous PET/MR imaging. *Mol Imaging Biol* 22:1208–1217
- Badawi RD, Shi H, Hu P, Chen S, Xu T, Price PM, Ding Y, Spencer BA, Nardo L, Liu W, Bao J, Jones T, Li H, Cherry SR (2019) First human imaging studies with the EXPLORER total-body PET scanner. *J Nucl Med* 60:299–303
- Surti S, Pantel AR, Karp JS (2020) Total body PET: why, how, what for. *IEEE Trans Radiat Plasma Med Sci* 4:283–292
- Berg E, Gill H, Marik J, Ogasawara A, Williams S, van Dongen G, Vugts D, Cherry SR, Tarantal AF (2020) Total-body PET and highly stable chelators together enable meaningful 89Zr-antibody PET studies up to 30 days after injection. *J Nucl Med* 61:453–460
- Ko GB, Kim KY, Yoon HS et al (2016) Evaluation of a silicon photomultiplier PET insert for simultaneous PET and MR imaging. *Med Phys* 43:72
- Kwon SI, Lee JS, Yoon HS, Ito M, Ko GB, Choi JY, Lee SH, Chan Song I, Jeong JM, Lee DS, Hong SJ (2011) Development of small-animal PET prototype using silicon photomultiplier (SiPM): initial results of phantom and animal imaging studies. *J Nucl Med* 52:572–579
- Park H, Ko GB, Lee JS (2017) Hybrid charge division multiplexing method for silicon photomultiplier based PET detectors. *Phys Med Biol* 62:4390–4405
- Ko GB, Lee JS (2017) Single transmission-line readout method for silicon photomultiplier based time-of-flight and depth-of-interaction PET. *Phys Med Biol* 62:2194–2207
- Yoon HS, Lee JS (2014) Bipolar analog signal multiplexing for position-sensitive PET block detectors. *Phys Med Biol* 59:7835–7846
- Son J-W, Won JY, Lee JS (2017) Evaluation of a FPGA-based real-time coincidence system for high count rate PET scanners. *IEEE Nucl Sci Symp Conf Rec*:1–3
- Hallen P, Schug D, Schulz V (2020) Comments on the NEMA NU 4-2008 standard on performance measurement of small animal positron emission tomographs. *EJNMMI Phys* 7:12
- He X, Wedekind F, Kroll T et al (2019) Image-derived input functions for quantification of A(1) adenosine receptors availability in mice brains using PET and [(18)F]CPFPX. *Front Physiol* 10:1617
- Kim SJ, Lee JS, Im KC, Kim SY, Park SA, Lee SJ, Oh SJ, Lee DS, Moon DH (2008) Kinetic modeling of 3'-deoxy-3'-18F-

- fluorothymidine for quantitative cell proliferation imaging in subcutaneous tumor models in mice. *J Nucl Med* 49:2057–2066
30. Lanz B, Poitry-Yamate C, Gruetter R (2014) Image-derived input function from the vena cava for ^{18}F -FDG PET studies in rats and mice. *J Nucl Med* 55:1380–1388
 31. Gsell W, Molinos C, Correcher C, Belderbos S, Wouters J, Junge S, Heidenreich M, Velde GV, Rezaei A, Nuyts J, Cawthorne C, Cleeren F, Nannan L, Deroose CM, Himmelreich U, Gonzalez AJ (2020) Characterization of a preclinical PET insert in a 7 Tesla MRI scanner: beyond NEMA testing. *Phys Med Biol* 65:245016
 32. Courteau A, McGrath J, Walker PM, Pegg R, Martin G, Garipov R, Doughty P, Cochet A, Brunotte F, Vrigneaud JM (2021) Performance evaluation and compatibility studies of a compact preclinical scanner for simultaneous PET/MR imaging at 7 Tesla. *IEEE Trans Med Imaging* 40:205–217

Publisher's Note Springer Nature remains neutral with regard to jurisdictional claims in published maps and institutional affiliations.